PHYSICAL REVIEW E **92**, 063007 (2015)

Cross-diffusion-driven hydrodynamic instabilities in a double-layer system: General classification and nonlinear simulations

M. A. Budroni[*]
Department of Chemistry and Pharmacy, University of Sassari, Sassari, Italy

(Received 10 August 2015; published 7 December 2015)

Cross diffusion, whereby a flux of a given species entrains the diffusive transport of another species, can trigger buoyancy-driven hydrodynamic instabilities at the interface of initially stable stratifications. Starting from a simple three-component case, we introduce a theoretical framework to classify cross-diffusion-induced hydrodynamic phenomena in two-layer stratifications under the action of the gravitational field. A cross-diffusion-convection (CDC) model is derived by coupling the fickian diffusion formalism to Stokes equations. In order to isolate the effect of cross-diffusion in the convective destabilization of a double-layer system, we impose a starting concentration jump of one species in the bottom layer while the other one is homogeneously distributed over the spatial domain. This initial configuration avoids the concurrence of classic Rayleigh-Taylor or differential-diffusion convective instabilities, and it also allows us to activate selectively the cross-diffusion feedback by which the heterogeneously distributed species influences the diffusive transport of the other species. We identify two types of hydrodynamic modes [the negative cross-diffusion-driven convection (NCC) and the positive cross-diffusion-driven convection (PCC)], corresponding to the sign of this operational cross-diffusion term. By studying the space-time density profiles along the gravitational axis we obtain analytical conditions for the onset of convection in terms of two important parameters only: the operational cross-diffusivity and the buoyancy ratio, giving the relative contribution of the two species to the global density. The general classification of the NCC and PCC scenarios in such parameter space is supported by numerical simulations of the fully nonlinear CDC problem. The resulting convective patterns compare favorably with recent experimental results found in microemulsion systems.

DOI: 10.1103/PhysRevE.92.063007 PACS number(s): 47.20.Bp, 47.20.Ma

I. INTRODUCTION

Diffusion plays a primary role in self-organization. When coupled to linear or nonlinear reactions, diffusive transport yields an impressive variety of patterns, ranging from fractal trees driven by diffusion-limited-aggregation (DLA) [1] to stationary (Turing patterns [2,3], Liesengang bands [4]) and traveling structures (chemical fronts [5,6] and waves [6–9]). First theorized in a seminal work by Alan Turing [2], the reaction-diffusion (RD) paradigm has been successfully used to describe emergent phenomena in biological and ecological systems [10], and thoroughly investigated by means of relatively simple model systems such as the well-known Belousov-Zhabotinsky (BZ) [11,12] and the chlorite-iodide-malonic acid (CIMA) reactions [13].

In the gravitational field, diffusion can also trigger convective patterns in initially stable stratifications, where a less dense solution is layered on top of a denser miscible solution [14–16]. Here, differential diffusion induces the interfacial destabilization of a double-layer system either when the component of lower layer diffuses faster than the upper one, or vice versa. The former mechanism, describing a double-diffusive (DD) instability, is well-known in oceanography, where salty warmer water overlies cold fresh water and salt fingering can occur because of the lower diffusion rate of the salt with respect to the heat [17]. By contrast, when the faster component is set on top, convective instability develops in time because the upper species, by diffusing downwards faster than the lower solute moves upwards, creates a density depletion area above the starting interface and an accumulation below it. The resulting convective structures, symmetrically positioned above and below the interface, are typical example of a double-layer-convection (DLC) instability [15,16,18,19].

Currently, one active frontier in pattern formation research concerns the study of novel structures, so-called chemohydrodynamic patterns [20], arising from the interplay among diffusion, chemical kinetics, and convection. Regarding double-layer configurations in vertically oriented reactors, it has been shown that reactive processes can severely modify the dynamics of the hydrodynamic patterns, switching from a symmetric fingering growth of nonreactive cases to nonsymmetric fingering if a rather simple $A + B \rightarrow C$ reaction is at play [21–24]. Vertically growing [25] and laterally traveling fingers [26] have been found in systems involving more complex autocatalytic or oscillatory kinetics localized at the interface between the two-layered reactants pools. In this context the competition between thermal- and solutal-related changes of density produced *in situ* by the reactive process must be taken into account [27,28] to explain composite structures which can be obtained with many active systems [29–37]. The antagonism among different contributions to convective flows induced by a reaction is also responsible for complex dynamics such as spatiotemporal oscillations [38,39], segmentation scenarios [40], and transition to chemical chaos [41–43] in autocatalytic fronts and waves propagating in vertically oriented reactors.

To date, most of the studies on chemohydrodynamic instabilities have focused on systems where the influence of cross-diffusive motions, i.e., fluxes induced in a given species by the presence of concentration gradients in the another ones [44], can be neglected. Much less conventional is the

---

[*] mabudroni@uniss.it

study of chemophysical processes in which cross-diffusion terms feature a dominating role. The dramatic effect of this contribution has been proved in nonreactive and reactive spatially distributed systems, both theoretically [45–52] and experimentally [49].

Nonetheless, cross-diffusion can also trigger an alternative path to buoyancy-driven convection in initially stable stratifications. The first example of such a mechanism was shown in a ternary system (polyvinylpyrrolidone(PVP)-dextran-H_2O) [53], where an aqueous solution of dextran was placed above a denser aqueous solution of equimolar dextran containing PVP. Starting from this buoyantly stable stratification, the diffusion of PVP from the lower solution to the upper one generates a coflux of dextran and, by means of this cross-diffusion feedback, causes the local inversion of the density profile around the initial interface with the consequent appearance of fingered patterns. This specific hydrodynamic scenario has been successively characterized and understood by means of further experimental investigations [54–57], and instability conditions were finally rationalized within a diffusion-convection modeling [58].

Recently [59], we have extended the array of possible experimental systems where cross-diffusion-driven convection can occur to the nonreactive AOT (sodium bis(2-ethylhexyl)sulfosuccinate Aerosol OT) microemulsions (AOT-ME). Microemulsions are liquid mixtures of an organic component (more often termed *oil*), water, and surfactant. Under the percolation threshold, ME appear at the nanoscale as dispersed spherical or elongated droplets where the surfactant constitutes a sort of membrane with the hydrophobic part oriented to the outer organic phase and the hydrophilic heads in contact with the inner aqueous phase segregated into the droplet.

We studied experimentally convective fingering growing symmetrically across the interface between two identical stratified AOT-ME in a Hele-Shaw cell [60]. The instability is promoted by a salt ($NaBrO_3$) added to the lower denser solution and free to diffuse toward the upper less-dense layer. This generates a positive coflux of both water and AOT and, in turn, produces a nonmonotonic density distribution along the gravitational field. The resulting convective scenario is similar to that observed with the PVP-dextran-H_2O system. Recently, we have shown that a similar but simplified version of the ME experiments with a three-component system (H_2O-AOT in octane) [60] is sufficient to explore an even richer spectrum of convective modes reminiscent of both DD or DLC hydrodynamic instabilities by changing the initial composition of the MEs along the gravitational axis.

Dispersed media such as ME, often characterized by large cross-diffusion terms due to excluded volume effects, are widely used to approach pattern formation in combination with the BZ system [61–68] and the coupling between cross-diffusion-driven convection and such reactive processes promises to be an unparalleled source for a new generation of chemohydrodynamic patterns. In order to pave the way toward this unexplored world, a robust and simplifying theory to the problem in the absence of any reaction is primarily needed.

The goal of this paper is to provide such a theoretical framework starting from the simplest three-component case (two solutes plus the solvent). A dimensionless model that couples the fickian diffusion with Stokes equations is used to describe cross-diffusion-driven hydrodynamic phenomena in the case of a double-layer initial configuration with a concentration jump in one of the solute across the two-layer contact line, while the other solute is set homogeneously over the whole spatial domain. The resulting density profile, featuring a less dense on top of a denser solution, is initially stable and allows us to isolate cross-diffusive effects in the convective destabilization. We show that our starting conditions can activate selectively specific elements of the cross-diffusion matrix, further reducing the complexity of the system description. Following a standard technique [15], analytic solutions to the pure cross-diffusion problem are used to reconstruct the space-time evolution of the density profiles along the gravitational field, by which the onset and the topology of convective patterns can be predicted. The analysis of the density profile morphology leads to a parametric classification of possible scenarios based on the sign of the cross-diffusion terms and on the relative contribution of the two species to the global density. The two types of cross-diffusion-driven hydrodynamic modes identified through the analytical procedure are reproduced and characterized by the numerical integration of the nonlinear CDC equations.

II. CDC MODEL

Consider a two-dimensional vertical slab of width L_X and height L_Z in a (X,Z) reference frame, where the gravitational acceleration $\bar{g} = (0,-g)$ is oriented downwards along the Z axis. The solution T of density ρ^T, containing the solute h with the initial concentration $C^T_{h,0}$ and the solute j with concentration $C^T_{j,0}$, is placed on top of the solution B, with concentration $C^B_{h,0} = C^T_{h,0}$, $C^B_{j,0} > C^T_{j,0}$ and density $\rho^B > \rho^T$ (see sketch in Fig. 1). In other words, the species h is homogeneously distributed over the spatial domain, while species j features a concentration jump downwards the gravitational axis.

The resulting double-layer stratification is stable to classic Rayleigh-Taylor or buoyancy-driven instabilities due to differential diffusion mechanisms, such as double-diffusion or double-layer-convection instabilities, and thus it is perfect to isolate the sole effect of cross diffusion on the system convective stability. Upon contact, the two miscible solutions, initially separated by a horizontal planar interface at $L_Z/2$,

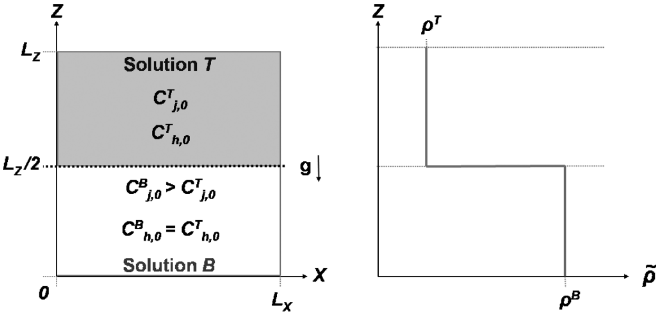

FIG. 1. Sketch of the two-dimensional stratification used to study cross-diffusion-driven convection. The initial distribution of the chemical solutes results in a step-function density profile.

start mixing by diffusion without inducing any thermal effect. The flux of each species is affected by concentration gradients in the other one as described by fickian equations where the cross-diffusive terms of the diffusion matrix **D** are taken into account explicitly.

In order to analyze the effect of cross diffusion in the onset of natural convection, diffusion equations are coupled to Stokes equations as

$$\partial_t C_j + (\mathbf{V}\cdot\nabla)C_j = D_{jj}\nabla^2 C_j + D_{jh}\nabla^2 C_h, \tag{1}$$

$$\partial_t C_h + (\mathbf{V}\cdot\nabla)C_h = D_{hj}\nabla^2 C_j + D_{hh}\nabla^2 C_h, \tag{2}$$

$$\nabla P = \mu\nabla^2\mathbf{V} - \tilde{\rho}(C_j,C_h)g\ \mathbf{1}_z, \tag{3}$$

$$\nabla\cdot\mathbf{V} = 0, \tag{4}$$

where the velocity field is modified by density changes according to the state equation:

$$\tilde{\rho}(C_j,C_h) = \rho^T\left[1 + \alpha_j\left(C_j - C^T_{j,0}\right) + \alpha_h\left(C_h - C^T_{h,0}\right)\right]. \tag{5}$$

This expansion relies on the assumption that species concentration slightly changes with respect to the initial composition of the reference top solution with density ρ^T and we can then admit a linear dependence of the global density $\tilde{\rho}$ upon the solute concentrations. In Eq. (5), $\alpha_j = \frac{1}{\rho^T}\frac{\partial\tilde{\rho}}{\partial C_j}$ and $\alpha_h = \frac{1}{\rho^T}\frac{\partial\tilde{\rho}}{\partial C_h}$ are the solutal expansion coefficients of the species j and h, respectively. In our framework, we consider the main coefficients (D_{jj}, D_{hh}) and the cross-diffusivity terms (D_{jh}, D_{hj}) relating the influence of the diffusive motion of the solute h to j (and vice versa) as constants and independent from the local species concentration [49,60].

Hydrodynamic equations are derived in the Boussinesq approximation, assuming the incompressibility of the fluid and that density changes only affect the gravitational term $\bar{g}\tilde{\rho}$ in Eq. (3). $\mathbf{V} = (U,V)$ is the velocity field, μ is the dynamic viscosity, and P is the pressure.

The model is reduced to a dimensionless form by introducing a characteristic system space scale L_0. The time and the velocity scales are then derived as $t_0 = L_0^2/D_{jj}$ and $v_0 = L_0/t_0$, while we use $p_0 = \mu/t_0$ and $\Delta C_{j,0} = (C^B_{j,0} - C^T_{j,0})$ as the pressure and concentration references, respectively. Moreover, we define the dimensionless density as $\rho(c_j,c_h,z) = (\tilde{\rho} - \rho^T)/(\rho^T\alpha_j\Delta C_{j,0})$. The introduction of the scaled variables $\{\tau = t/t_0,\ (x,z) = (X,Z)/L_0,\ (c_j,c_h) = (C_j - C^T_{j,0}, C_h - C^T_{h,0})/\Delta C_{j,0},\ \mathbf{v} = \mathbf{V}/v_0,\ p = P/p_0\}$ leads to the following dimensionless equations:

$$\partial_\tau c_j + (\mathbf{v}\cdot\nabla)c_j = \nabla^2 c_j + \delta_{jh}\nabla^2 c_h, \tag{6}$$

$$\partial_\tau c_h + (\mathbf{v}\cdot\nabla)c_h = \delta_{hj}\nabla^2 c_j + \delta_{hh}\nabla^2 c_h, \tag{7}$$

$$\nabla p = \nabla^2\mathbf{v} - (R\,c_h + c_j)\mathbf{1}_z, \tag{8}$$

$$\nabla\cdot\mathbf{v} = 0, \tag{9}$$

where the dimensionless parameter $\delta_{hh} = D_{hh}/D_{jj}$ is the ratio between the main molecular diffusion coefficient of solute h to that of j. Similarly, $(\delta_{jh},\delta_{hj}) = (D_{jh},D_{hj})/D_{jj}$. The buoyancy ratio

$$R = \frac{\alpha_h}{\alpha_j} \tag{10}$$

quantifies the relative contribution of the initially homogeneous species to the density with respect to species j, featuring the initial concentration jump. More in detail, R measures how a change in h concentration can modify the density as compared to the same variation of j concentration. This parameter is conveniently used for expressing the dimensionless density ρ as described below in Sec. III. Here R is assumed as a positive quantity (i.e., the solution density increases upon the increment of solute concentrations).

Equations (6)–(9) can be written in the $(\omega - \psi)$ form by taking the curl of both sides of Eq. (8). The term ∇p is eliminated and, by defining the *vorticity* $\omega = \nabla\times\mathbf{v}$ and the *stream function*, ψ, through the relations ($u = \partial_z\psi$, $v = -\partial_x\psi$), the cross-diffusion-convection (CDC) model reads

$$\frac{\partial c_j}{\partial\tau} + \left(\frac{\partial\psi}{\partial z}\frac{\partial c_j}{\partial x} - \frac{\partial\psi}{\partial x}\frac{\partial c_j}{\partial z}\right) = \nabla^2 c_j + \delta_{jh}\nabla^2 c_h, \tag{11}$$

$$\frac{\partial c_h}{\partial\tau} + \left(\frac{\partial\psi}{\partial z}\frac{\partial c_h}{\partial x} - \frac{\partial\psi}{\partial x}\frac{\partial c_h}{\partial z}\right) = \delta_{hj}\nabla^2 c_j + \delta_{hh}\nabla^2 c_h, \tag{12}$$

$$\nabla^2\omega = R\frac{\partial c_h}{\partial x} + \frac{\partial c_j}{\partial x}, \tag{13}$$

$$\frac{\partial^2\psi}{\partial x^2} + \frac{\partial^2\psi}{\partial z^2} = -\omega. \tag{14}$$

The problem is closed through the initial conditions

$$\begin{aligned} \forall\ x : (c_j,c_h,\psi) &= (1,0,0) \quad \text{for} \quad z \leqslant z_0, \\ (c_j,c_h,\psi) &= (0,0,0) \quad \text{for} \quad z > z_0. \end{aligned} \tag{15}$$

By following the above procedure, the model can be straightforwardly extended to a n-component system and specialized to different cases on the basis of which solute features the initial concentration jump while the others are homogeneously distributed along the spatial domain.

III. DENSITY-PROFILE-BASED CLASSIFICATION OF THE INSTABILITY SCENARIOS

The double-layer initial condition represents a key specificity of the cross-diffusion problem under study. Before the onset of an instability, we can assume that the flow is at rest and the concentration profiles of the species do not vary along the x direction. The initial evolution of the concentration fields can be thus followed along the vertical coordinate z and described by means of the cross-diffusion equations (i.e., Eqs. (11) and (12) with $\psi = 0$). The information about the cross-diffusion effect on the dynamics is embedded in the matrix $\boldsymbol{\delta}$. Due to the sharp initial gradient imposed to the concentration profile $c_j(z,0)$, the cross-diffusion term δ_{hj} dominates the initial part of the dynamics while the other off-diagonal cross-diffusivity, δ_{jh}, plays a negligible role.

We can then isolate two different cross-diffusion paths depending upon the influence of the species featuring the concentration jump on the initially homogeneously distributed species, as controlled by the sign of the cross-diffusion coefficient δ_{hj}. If δ_{hj} is positive, the diffusion of species j from the bottom to the upper layer in response to the initial

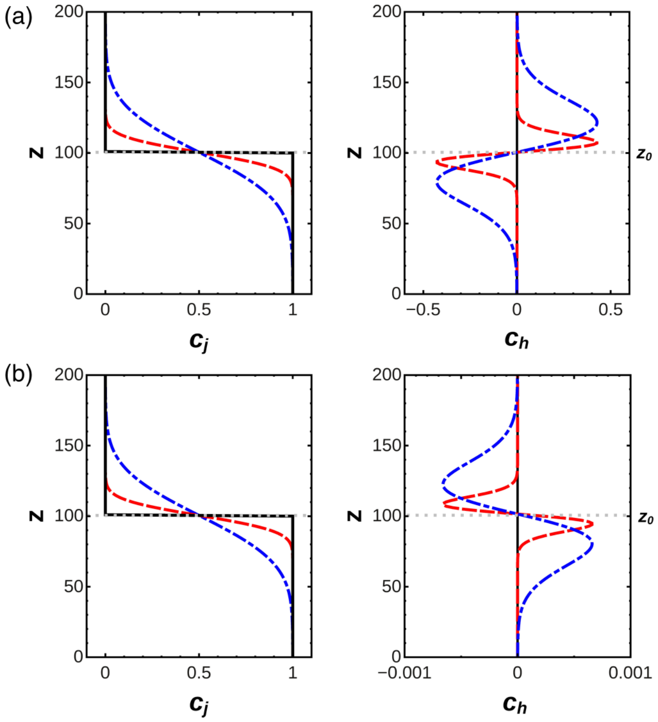

FIG. 2. (Color online) Typical spatiotemporal evolution of the dimensionless concentration profiles $c_j(z,\tau)$ and $c_h(z,\tau)$ when (a) $\delta_{hj} > 0$ (4.70) or (b) $\delta_{hj} < 0$ (-0.01). In each panel solid black lines describe the initial distribution of the species, while dashed red and dotted blue profiles depict progressively the spatial concentration profiles at successive times.

concentration gradient generates a coflux in h [Fig. 2(a)] and, as a result, the initially flat concentration profile $c_h(z,\tau)$ develops a nonmonotonic shape with a local maximum and a minimum symmetrically located above and below the initial interface, respectively. By contrast, the propagation of solute j toward the upper layer triggers a counterflux in h if δ_{hj} is negative. In the concentration profile $c_h(z,\tau)$ this produces a local depletion area in the upper layer and an accumulation just below the initial interface located at $z_0 = L_Z/(2L_0)$ [Fig. 2(b)]. We clearly observe an inversion in the morphology of the concentration profiles when switching from a positive to a negative δ_{hj} and the relative intensity of the concentration extrema developing in time along $c_h(z,\tau)$ reflects the magnitude of δ_{hj} itself.

The fact that only δ_{hj} is initially at play greatly simplifies the analytical approach to our cross-diffusion problem. As a matter of fact, the exact solutions to the concentration profiles, which present the general form [47]

$$c_j(z,\tau) = A_{jj}G_j + A_{jh}G_h, \tag{16}$$

$$c_h(z,\tau) = A_{hj}G_j + A_{hh}G_h, \tag{17}$$

(where the function G for the ith species reads $G_i = \frac{1}{2}\mathrm{erfc}[(z-z_0)/\sqrt{(4\sigma_i t)}]$, σ_i are the eigenvalues of the matrix $\boldsymbol{\delta}$, the constants $A_{jj} = (\delta_{jj} - \sigma_h)/(\sigma_j - \sigma_h)$, $A_{jh} = (\sigma_j - \delta_{jj})/(\sigma_j - \sigma_h)$, $A_{hj} = -\delta_{hj}/(\sigma_h - \sigma_j)$ and $A_{hh} = \delta_{hj}/(\sigma_h - \sigma_j)$ are obtained by substituting G_i in Eq. (17) and by taking into account the initial conditions $A_{jj} + A_{jh} = 1$ and $A_{hj} + A_{hh} = 0$ at $z = z_0\ \forall t$), reduce to

$$c_j(z,\tau) = \frac{1}{2}\mathrm{erfc}\left(\frac{(z-z_0)}{\sqrt{4\tau}}\right), \tag{18}$$

$$c_h(z,\tau) = \frac{-\delta_{hj}}{2(\delta_{hh}-1)}\mathrm{erfc}\left(\frac{(z-z_0)}{\sqrt{4\tau}}\right) + \frac{\delta_{hj}}{2(\delta_{hh}-1)}\mathrm{erfc}\left(\frac{(z-z_0)}{\sqrt{4\delta_{hh}\tau}}\right), \tag{19}$$

since in the limit case $\delta_{jh} = 0$, σ_j and σ_h coincide with δ_{jj} and δ_{hh}, respectively, and the constants $A_{jj} = 1$, $A_{jh} = 0$, $A_{hj} = -\delta_{hj}/(\delta_{hh} - 1)$, and $A_{hh} = -A_{hj}$.

The concentration profiles $c_j(z,\tau)$ and $c_h(z,\tau)$ constitute the basis set to reconstruct the evolution of the dimensionless density profiles according to the dimensionless state equation [corresponding to Eq. (5) for the dimensional problem],

$$\rho(z,\tau) = c_j(z,\tau) + R\,c_h(z,\tau), \tag{20}$$

i.e.,

$$\rho(z,\tau) = \left(\frac{1}{2(\delta_{hh}-1)}\right)\left[\left(\delta_{hh} - 1 - \delta_{hj}R\right) \times \mathrm{erfc}\left(\frac{(z-z_0)}{\sqrt{4\tau}}\right) + \delta_{hj}R\ \mathrm{erfc}\left(\frac{(z-z_0)}{\sqrt{4\delta_{hh}\tau}}\right)\right]. \tag{21}$$

Equation (20) implies that if the relative contribution of species h to the global density (measured by R) is large enough, the nonmonotonic concentration profile that characterizes this species impacts the morphology of the dimensionless density distribution along the gravitational axis. Due to buoyancy forces, nonmonotonic density profiles can be responsible for the convective destabilization of a double-layer system as a local maximum of $\rho(z,\tau)$ indicates a buoyantly unstable situation in which denser fluid locally overlies a less-dense medium. By isolating the parametric constraints that determine the development of extrema points along $\rho(z,\tau)$ and by analyzing its shape, we can predict the emergence and the qualitative topology of convective patterns [15,23,24,59,69].

More specifically, by studying where the gradient of $\rho(z)$,

$$\partial\rho_z(z,\tau) = \left(\frac{1}{\sqrt{4\pi\tau}\,(\delta_{hh}-1)}\right) \times \left[(1 + \delta_{hj}R - \delta_{hh})\exp\left(-\frac{(z-z_0)^2}{4\tau}\right) - \left(\frac{\delta_{hj}R}{\sqrt{\delta_{hh}}}\right)\exp\left(-\frac{(z-z_0)^2}{4\delta_{hh}\tau}\right)\right], \tag{22}$$

is locally zero, we obtain that $\rho(z,\tau)$ presents symmetric extrema with respect to $z = z_0$ when z satisfies

$$(z-z_0)^2 = \frac{4\,\delta_{hh}\tau}{(1-\delta_{hh})}\ln\left(\frac{\delta_{hj}R}{(1+\delta_{hj}R-\delta_{hh})\sqrt{\delta_{hh}}}\right). \tag{23}$$

A nonmonotonic density profile, characterized by a local maximum overlying a minimum across z_0 (also a signature of a DD-type instability [15]), develops if the density gradient at the interface $\partial\rho_z(z)|_{z=z_0}$ is positive; vice versa a DLC-type density profile [15] (with a reversed ρ shape with respect to the DD-type case) is expected if $\partial\rho_z(z)|_{z=z_0}$ is negative.

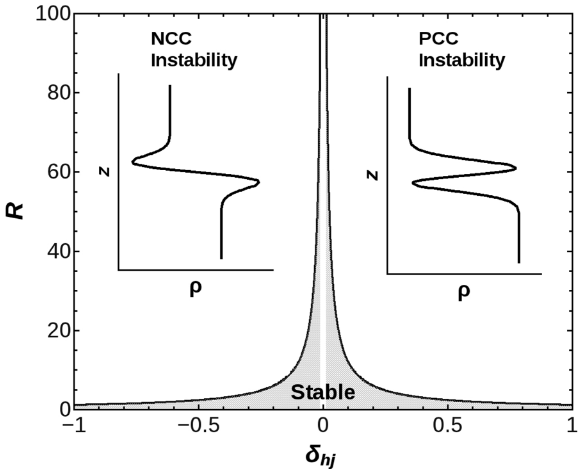

FIG. 3. Classification of cross-diffusion-driven scenarios in the (δ_{hj},R) parameter space based on the analysis of the dimensionless density profiles. The symmetric hyperbolic curves describe the instability threshold relating R to δ_{hj}. The shadowed area identifies the domain where the system is buoyantly stable as the related density profile increases monotonically downwards the gravitational axis. PPC and NCC scenarios occur in the domain of positive and negative δ_{hj}, respectively.

By taking into account the sign of $\partial\rho_z(z)|_{z=z_0}$ and the existence of the logarithm in Eq. (23), we find that a nonmonotonic density profile across z_0 generally occurs when

$$R > \frac{\sqrt{\delta_{hh}}(1+\sqrt{\delta_{hh}})}{|\delta_{hj}|}. \tag{24}$$

Thanks to Eq. (24), the possible instability scenarios can be classified in the reduced parameter space (δ_{hj}, R). As illustrated in Fig. 3, this shows three main regions. Under the hyperbolic curves relating R to the operational cross-diffusivity, δ_{hj} (shadowed area in Fig. 3), the system is buoyantly stable to a cross-diffusion-driven hydrodynamic instability. In this region the dimensionless density profile describing the system increases monotonically downwards z. The regions where nonmonotonic density profiles can develop, with the characteristic morphologies shown in Fig. 3, extend above the black curve. The sign of δ_{hj} discriminates the domains where positive cross-diffusion-driven convection, PCC scenarios ($\partial\rho_z(z)|_{z=z_0} > 0$, $\delta_{hj} > 0$), or negative cross-diffusion-driven convection, NCC scenarios ($\partial\rho_z(z)|_{z=z_0} < 0$, $\delta_{hj} < 0$), are to be expected. The instability threshold $R = f(\delta_{hj})$ is clearly symmetric with respect to the ordinate axis, $\delta_{hj} = 0$. The curves describing the system marginal stability shift to lower values of R when decreasing δ_{hh}, indicating that a high main-diffusivity of the initially homogeneously distributed species plays a stabilizing effect in the onset of cross-diffusion-driven convection.

IV. NONLINEAR SIMULATIONS

In order to complement the results obtained from the density-profile-based classification, we perform nonlinear simulations of Eqs. (11)–(14). This allows us to determine the onset time of the instability, to follow the dynamics by which fingering nucleates and grows, and to characterize the modes that dominate the convective patterns.

A. Numerical details

Equations (11)–(14) are solved by means of the alternating direction implicit method (ADI) [70], using a squared spatial domain $L_x = L_z = 200$, and equal meshing for space integration along the horizontal and vertical spatial directions ($hx = hz = 0.5$). We apply no-flux boundary conditions for the concentration field of the chemical species at the four solid boundaries of the two-dimensional reactor while no-slip boundary conditions, required at rigid walls for the flow, apply to the stream function. Simulations are run using the time step $ht = 1 \times 10^{-3}$, which was tested to give convergent solutions. The problem is finally defined by the initial conditions Eq. (15). According to the previous discussion in Sec. III (Fig. 3), positive and negative values of δ_{hj} should be used in order to simulate a PCC and a NCC hydrodynamic scenario, respectively. As illustrative examples we consider values of the δ_{hj} with the same order of magnitude characterizing cross-diffusion terms in microemulsion systems recently studied as model systems to approach experimentally cross-diffusion-driven hydrodynamic instabilities [60]. We then analyze the system dynamics for different values of the buoyancy ratio R for which condition Eq. (24) is satisfied. We also checked that no instability develops for values within the stable region of the parameter space (δ_{hj}, R).

B. Results

Let us fist give an overview on the phenomenology of the two possible instabilities. In the upper panel of Fig. 4 we show the dynamical destabilization of the two-layer interface due to a PCC mechanism while in the lower panel is illustrated a typical NCC scenario. The two arrays of snapshots follow the spatiotemporal evolution of the instability by mapping the vorticity $\omega(x,z,\tau)$ over the simulation spatial domain. In both cases, the unstable area starts from the border of the spatial domain where a numerical perturbation can break the symmetry and extends along the horizontal direction. As convective fingers form, they grow vertically along the

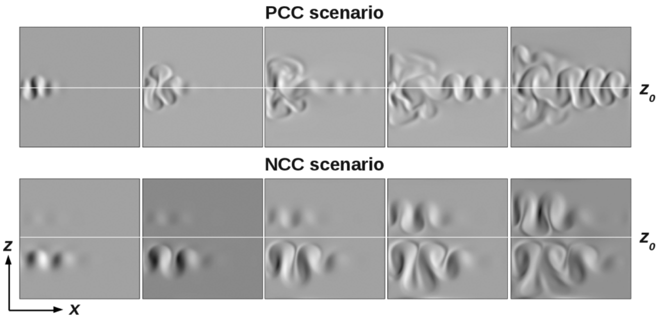

FIG. 4. Typical spatiotemporal evolution of a PCC (upper panel) and a NCC (lower panel) instability. The PCC scenario is obtained with $\delta_{hj} = 4$ and $R = 0.5$, while the NCC scenario with $\delta_{hj} = -0.01$ and $R = 100$. Each sequence of snapshots maps the vorticity $\omega(x,z,\tau)$ over the simulation spatial domain. The amplitude of $\omega(x,z,\tau)$ in the plots ranges between -10 (dark areas) and 10 (bright areas).

gravitational axis but they also undergo a slow drifting toward the side where the instability nucleates, progressively merging with preexisting fingers. This is due to the delayed formation of new fingers, which experience the effect of residual flows.

The PCC scenario is induced by the positive cross-diffusion term δ_{hj}. As previously shown in Fig. 2(a), solute j diffuses from the bottom to the upper layer due to the initial gradient and triggers a nonmonotonic distribution $c_h(z,\tau)$ featuring a local density maximum over a minimum downwards z, symmetrically located around z_0. If the buoyancy ratio R meets the requirement of Eq. (24), a nonmonotonic density profile with the morphology shown in the positive domain of Fig. 3 can take place. In the presence of the gravitational field, this induces a hydrodynamic instability reminiscent of a DD scenario [15], which symmetrically develops toward the upper and the lower layer.

The NCC-type convective pattern is determined by a negative cross-diffusion coefficient δ_{hj}. Here the motion of solute j develops the nonmonotonic concentration profile $c_h(z,\tau)$ shown in Fig. 2(b). As a consequence, a density profiles with the shape described in Fig. 3 for negative δ_{hj} can develop, provided that R satisfies the instability condition of Eq. (24). On the basis of the morphology of this density profile, we can better interpret the convective patterns shown in Fig. 4 (lower panel), with fingers localized in the top and the bottom layer. During the development of the instability, the initial interface is not deformed because of the formation of the density maximum located below the initial interface. On the one side, this acts as a density barrier preventing the finger growth from the top to the bottom layer; on the other hand, it is the source for convective fingering in the bottom layer. The NCC scenario reminds the typical patterns arising from a DLC instability [15].

C. Characterization

The main features of the cross-diffusion-driven convective scenarios, namely the time needed for the onset of the fingering instability (t^*) and the dominant wavelength (λ^*), are analyzed in Figs. 5 and 6 as a function of R, for three different values of δ_{hj}. The dominating modes (and the corresponding λ^*) characterizing these instabilities have been calculated from the fast Fourier transform of the transverse profile of the vorticity along the horizontal interface at $z = z_0$, when the convective patterns are fully developed along the whole x axis.

For both classes of instability the system becomes convectively more unstable by increasing the buoyancy ratio which corresponds to intensifying the density extrema along the non-monotonic profiles shown in Fig. 3. In turn, both λ^* and t^* decrease while increasing R. It is worth noticing that both observables follow a linear trend when plotted in the log-log scale, indicating a power-law relation linking these hydrodynamic properties to the parameter R. In particular, irrespectively of the convective scenario at play and the value of δ_{hj}, the wavelength scales as $\lambda^* = R^{\beta}$ with $\beta = -0.30 \pm 0.02$, while the average exponent $\beta = -0.70 \pm 0.02$ recurs for the instability onset time.

The mixing length (L_m), which measures the extent of the fingering area in the course of time, has been also quantified on the basis of the concentration profile $c_h(x,z,\tau)$ transversely averaged over the x direction: $\langle c_h\rangle(z,\tau) = \frac{1}{L_x}\int_0^{L_x} c_h(x,z,\tau)\, dx$. The fingering area coincides roughly with the nonmonotonic area growing around z_0 in $\langle c_h\rangle(z,\tau)$. The tip ($z_t$) and the back ($z_b$) of this growing nonmonotonic area are, respectively, located as the sup $\{z\} : |\langle c_h\rangle(z,\tau)| > \epsilon_0$ and the inf $\{z\} : |\langle c_h\rangle(z,\tau)| > \epsilon_0$, where the concentration reference $\epsilon_0 \ll 1$. $L_m = z_t - z_b$ defines the distance between these two endpoints.

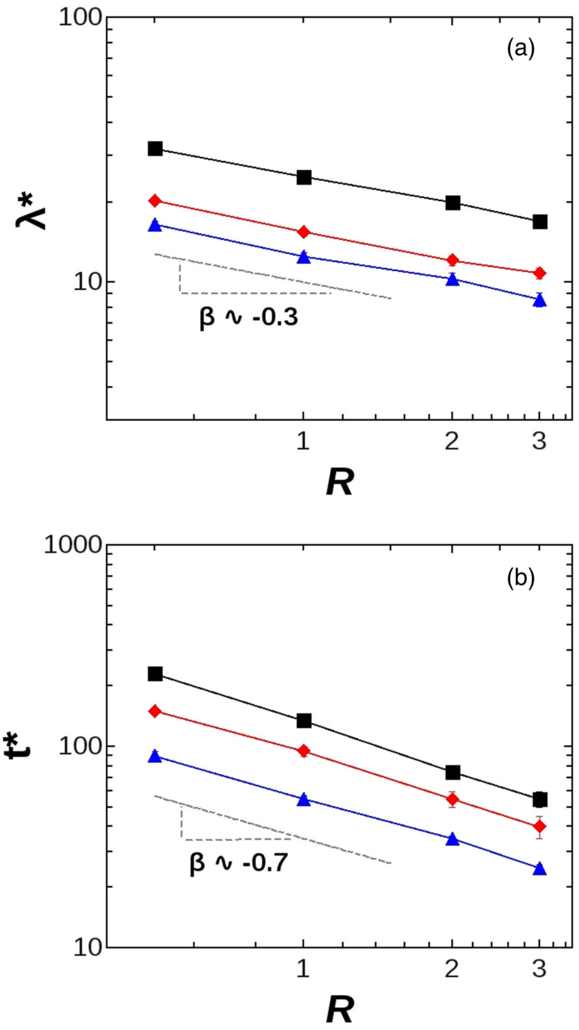

FIG. 5. (Color online) Analysis of the PCC convective patterns by means of (a) the characteristic wavelength, λ^*, and (b) the onset time, t^*, as a function of the buoyancy ratio R. For the δ_{hj} values considered (black ■ = 4.73; red ♦ = 9.46, blue ▲ = 18.92), λ^* follows a common power-law scaling described by the exponent $\beta \sim -0.3$. This is also true for t^*, showing $\beta \sim -0.7$.

Figure 7(a) compares the spatiotemporal evolution of z_t and z_b at four different values of R, for the PCC instability; the corresponding L_m trends are plotted as a function of the time in Fig. 7(b). An analogous characterization is presented in Fig. 8 for NCC scenarios. Both the PPC and the NCC dynamics show an initial diffusive transient where z_t, z_b (and, consequently, L_m) increase monotonically, scaling as the square root of the time. The length of this induction period coincides with t^* and, thus, decreases exponentially with R as shown in Figs. 5 and 6. When the system undergoes the

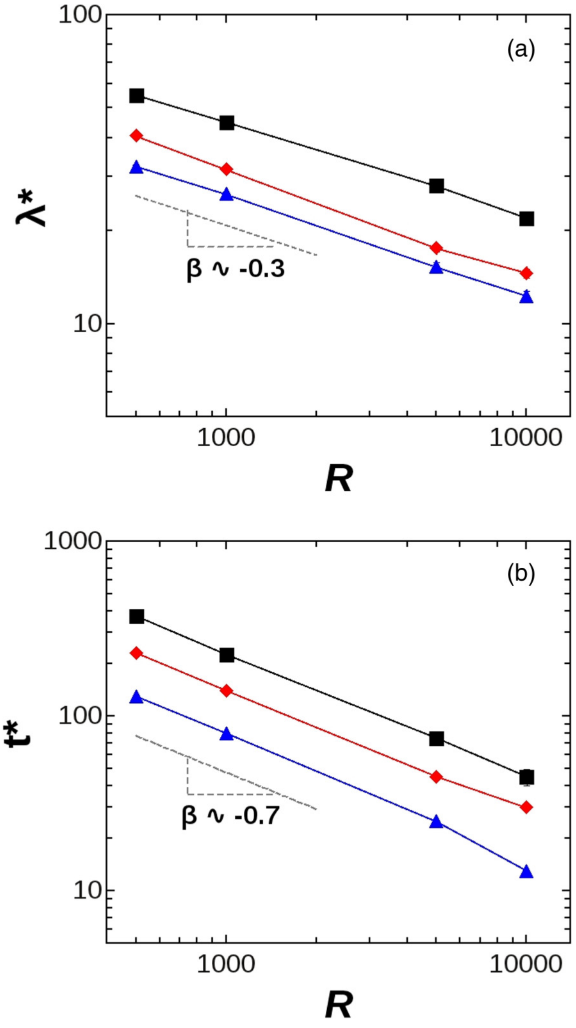

FIG. 6. (Color online) Analysis of the NCC convective patterns by means of (a) the characteristic wavelength, λ^*, and (b) the onset time, t^*, as a function of the buoyancy ratio R. For the δ_{hj} values considered (black ■ $= -0.01$; red ♦ $= -0.02$, blue ▲ $= -0.04$), λ^* follows a common power-law scaling described by the exponent $\beta \sim -0.3$. This is also true for t^*, showing $\beta \sim -0.7$. Note that the average values of β correspond to the scaling exponents characterizing the PCC scenario.

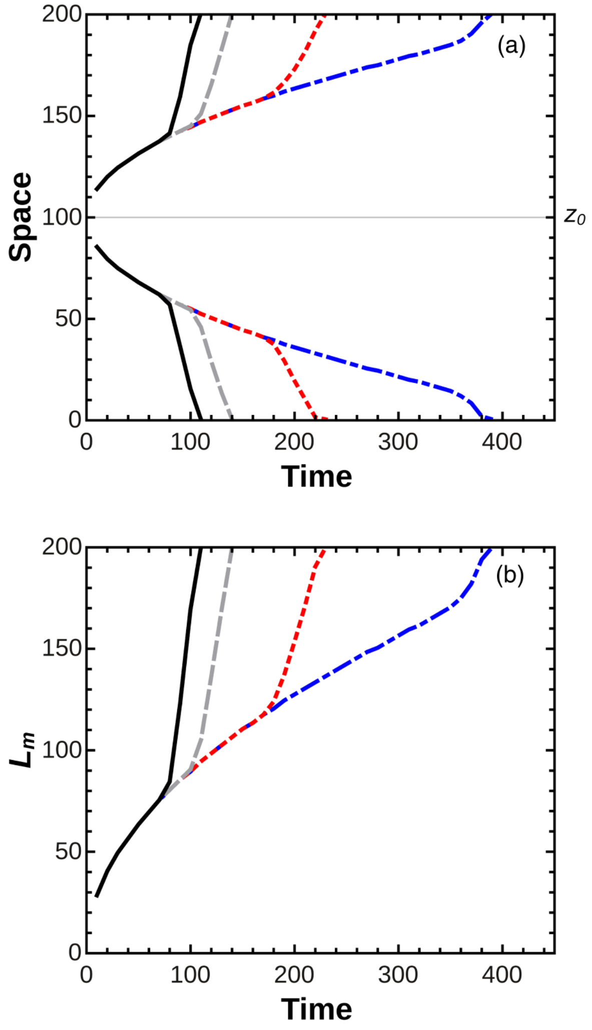

FIG. 7. (Color online) Spatiotemporal characterization of PCC hydrodynamic instabilities when R equals 0.5 (dash-dotted blue curve), 1 (dotted red curve), 2 (dashed gray curve), and 3 (solid black curve). In panel (a) we plot the evolution of the tip ($z_t > z_0$) and the back ($z_b < z_0$) of the fingering area; in panel (b) we follow as a function of the time the corresponding mixing length, L_m.

hydrodynamic instability, $z_t(\tau)$, $z_b(\tau)$, and $L_m(\tau)$ switch to a linear behavior. The slope of $L_m(\tau)$ in the linear regime gives an averaged value of the instability growth rate, which decreases slightly by lowering R. While the PCC scenarios exhibit a highly symmetric spatiotemporal development with regard to the initial interface [see Fig. 7(a)], we can observe in Fig. 8(a) that the NCC growth is more enhanced in the bottom layer, where the divergence from the diffusive regime takes place earlier as compared to the upper layer.

V. CONCLUDING DISCUSSION

Cross-diffusion can sustain a wealth of self-organized patterns, including convective fingering. In this paper we have discussed a general method to trigger and control pure cross-diffusion-driven hydrodynamic instabilities by using a double-layer three-component system in which a concentration jump is imposed initially to one solute while the other is homogeneously distributed over the spatial domain. Depending upon the sign of the operational cross-diffusion term, which ties the motion of the initially heterogeneous species to the homogeneous one, we can have two main scenarios. The NCC scenarios occur because the species free to diffuse from the bottom to the upper layer induces a counterflux in the other species controlled by a negative cross diffusivity and, as a consequence, a density depletion and an accumulation area develop above and below the initial interface, respectively; vice versa, an interface deforms into a PCC fingering when the bottom-top diffusing species produces a coflux of the other species via a positive cross diffusivity δ_{hj}. In turn, this generates in the course of time a local density maximum overlying a density minimum. The NCC and PCC patterns show strong similarities with the well-known DLC and DD

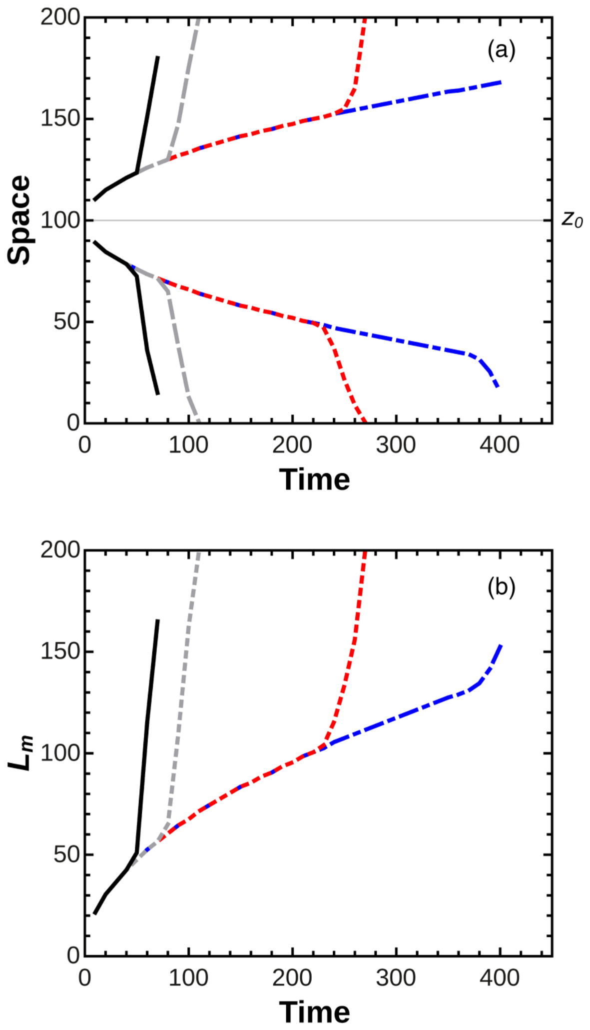

FIG. 8. (Color online) Spatiotemporal characterization of NCC hydrodynamic instabilities when R is fixed to 500 (dash-dotted blue curve), 1000 (dotted red curve), 5000 (dashed gray curve), and 10 000 (solid black curve). As described in the caption of Fig. 7, in panel (a) we plot the temporal evolution of the tip ($z_t > z_0$) and the back ($z_b < z_0$) of the fingering area; in panel (b) we follow as a function of the time the corresponding mixing length, L_m.

instabilities, respectively, as they are described by isomorphic density profiles along the gravitational axis.

Note that both the NCC and the PCC scenarios can be separately induced in the same three-component system provided that the two off-diagonal elements of the diffusion matrix present opposite sign. Based on the study of the evolution of analytical density profiles we have parametrically isolated instability conditions and identified the regions for the two possible convective scenarios in a simple parameter space consisting of the cross diffusivity at play, δ_{hj}, and the buoyancy ratio, R. Nonlinear simulations of our CDC model confirm the validity of this general classification and the characterization of the main hydrodynamic properties of cross-diffusion-driven convective patterns reveals a power-law scaling of the instability onset time and characteristic wavelength as a function of R. Interestingly, universal scaling exponents are found in both NCC and PCC scenarios for λ^* ($\beta \sim -0.3$) and t^* ($\beta \sim -0.7$).

The spatiotemporal evolutions and the characteristics of the convective patterns obtained by numerical solution of the CDC equations compare favorably with experimental results recently reported for AOT-ME systems studied in a vertically oriented Hele-Shaw cell [59,60]. In their simplest formulation, these experiments involve water (solute 1) and AOT (solute 2) as the two species giving cross-diffusive interplay while the octane features the solvent. In the experimental conditions considered (composition, temperature), the diffusion matrix of this system show a cross-diffusion term δ_{12} (by which the motion of the AOT influences the diffusion of the water) large and positive, while δ_{21} is small and negative [60]. In excellent agreement with the analytical prediction and numerical simulations discussed in this paper, the experiments show NCC scenarios when a starting concentration jump is set in the water spatial profile (while [AOT] is constant over the whole reactor). To our best knowledge this is the first experimental example of this convective mode. By contrast, PCC patterns develop with an initial concentration jump in the AOT (keeping homogeneous the initial distribution of water).

Our approach can be employed to design new experiments where cross-diffusion-driven convection can occur in three-component systems but can also be straightforwardly extended to n-component cases. More importantly, this is a benchmark study for future experimental investigations of systems where cross-diffusion-driven convection is coupled with chemical reactions to yield new chemohydrodynamic patterns.

Finally, understanding the mechanisms and the conditions for a hydrodynamic instability is crucial to control undesired phenomena (such as fingering in oil extraction [71,72]) but also to promote rapid mixing and optimized transport when necessary (for instance in convective techniques for CO_2 sequestration [24,73]). In this context, cross-diffusion convection can be very efficient and deepening its possible impact in many issues of applied relevance is one of the main goals of future work.

ACKNOWLEDGMENTS

I thank Prof. A. De Wit, Dr. F. Rossi, and Prof. T. J. Steger for valuable suggestions and fruitful discussions. Regione Sardegna is gratefully acknowledged for financial support in the framework of “Asse IV Capitale Umano, Obiettivo Operativo l.3 Linea di Attività l.3.1 del P.O.R. Sardegna F.S.E. 2007/2013-Progetti in forma associata e/o partenariale C.U.P. E85E12000060009.”

[1] T. A. Witten, Jr. and L. M. Sander, Phys. Rev. Lett. **47**, 1400 (1981).

[2] A. M. Turing, Philos. Trans. R. Soc. London **237**, 37 (1952).

[3] V. Castets, E. Dulos, J. Boissonade, and P. De Kepper, Phys. Rev. Lett. **64**, 2953 (1990).

[4] R. E. Liesegang, Naturwissenschaftliche Wochenschrift **11**, 353 (1896).

[5] L. Gálfi and Z. Rácz, Phys. Rev. A **38**, 3151 (1988).
[6] I. R. Epstein and J. A. Pojman, *An Introduction to Nonlinear Chemical Dynamics* (Oxford University Press, Oxford, 1998).
[7] R. J. Field and M. Burger, *Oscillations and Traveling Waves in Chemical Systems* (Wiley, New York, 1985).
[8] J. J. Tyson and J. P. Keener, Physica D **32**, 327 (1988).
[9] M. A. Budroni and F. Rossi, J. Phys. Chem. C **119**, 9411 (2015).
[10] J. D. Murray, *Mathematical Biology, I* (Springer-Verlag, New York, 2002).
[11] B. P. Belousov, in *Sbornik Referatov po Radiatsonno Meditsine* (Medgiz, Moscow, 1958), pp. 145–147.
[12] A. M. Zhabotinsky, Proc. Acad. Sci. USSR **157**, 392 (1964).
[13] I. Lengyel, G. Ribai, and I. R. Epstein, J. Am. Chem. Soc. **112**, 9104 (1990).
[14] J. S. Turner, *Buoyancy Effects in Fluids* (Cambridge University Press, New York, 1979).
[15] P. M. J. Trevelyan, C. Almarcha, and A. De Wit, J. Fluid Mech. **670**, 38 (2011).
[16] J. Carballido-Landeira, P. M. J. Trevelyan, C. Almarcha, and A. De Wit, Phys. Fluids **25**, 024107 (2013).
[17] H. Stommel, A. B. Arons, and D. Blanchard, Deep-Sea Res. **3**, 152 (1956).
[18] H. E. Huppert and J. S. Turner, J. Fluid Mech. **106**, 299 (1981).
[19] R. W. Griffiths, J. Fluid Mech. **102**, 221 (1981).
[20] A. De Wit, K. Eckert, and S. Kalliadasis, Chaos **22**, 037101 (2012).
[21] C. Almarcha, P. M. J. Trevelyan, P. Grosfils, and A. De Wit, Phys. Rev. Lett. **104**, 044501 (2010).
[22] C. Almarcha, Y. R'Honi, Y. De Decker, P. M. J. Trevelyan, K. Eckert, and A. De Wit, J. Phys. Chem. B **115**, 9739 (2011).
[23] L. Lemaigre, M. A. Budroni, L. A. Riolfo, P. Grosfils, and A. De Wit, Phys. Fluids **25**, 014103 (2013).
[24] M. A. Budroni, L. A. Riolfo, L. Lemaigre, F. Rossi, M. Rustici, and A. De Wit, J. Phys. Chem. Lett. **5**, 875 (2014).
[25] T. Bánsági, Jr., D. Horváth, Á. Tóth, J. Yang, S. Kalliadasis, and A. De Wit, Phys. Rev. E **68**, 055301 (2003).
[26] D. Escala, M. A. Budroni, J. Carballido-Landeira, A. De Wit, and A. Munuzuri, J. Phys. Chem. Lett. **5**, 413 (2014).
[27] J. A. Pojman and I. R. Epstein, J. Phys. Chem. **94**, 4966 (1990).
[28] S. Kalliadasis, J. Yang, and A. De Wit, Phys. Fluids **16**, 1395 (2004).
[29] G. Bazsa and I. R. Epstein, J. Phys. Chem. **89**, 3050 (1985).
[30] J. A. Pojman, I. R. Epstein, T. J. McManus, and K. Showalter, J. Phys. Chem. **95**, 1299 (1991).
[31] I. Nagypál, G. Bazsa, and I. R. Epstein, J. Am. Chem. Soc. **108**, 3635 (1986).
[32] I. Nagy and J. A. Pojman, J. Phys. Chem. **97**, 3443 (1993).
[33] C. Chinake and R. Simoyi, J. Phys. Chem. **98**, 4012 (1994).
[34] A. Keresztessy, I. Nagy, G. Bazsa, and J. A. Pojman, J. Phys. Chem. **99**, 5379 (1995).
[35] A. Komlosi, I. Nagy, G. Bazsa, and J. A. Pojman, J. Phys. Chem. **102**, 9136 (1998).
[36] J. A. Pojman, R. Craven, A. Khan, and W. West, J. Phys. Chem. **96**, 7466 (1992).
[37] F. Rossi and M. L. Turco Liveri, Ecol. Model. **220**, 1857 (2009).
[38] L. Rongy, P. Assemat, and A. De Wit, Chaos **22**, 037106 (2012).
[39] M. A. Budroni, L. Rongy, and A. De Wit, Phys. Chem. Chem. Phys. **14**, 14619 (2012).
[40] F. Rossi, M. A. Budroni, N. Marchettini, and J. Carballido-Landeira, Chaos: Interdisc. J. Nonlin. Sci. **22**, 037109 (2012).
[41] L. Ciotti, M. A. Budroni, M. Masia, N. Marchettini, and M. Rustici, Chem. Phys. Lett. **512**, 290 (2011).
[42] N. Marchettini, M. A. Budroni, F. Rossi, M. Masia, M. L. Turco Liveri, and M. Rustici, Phys. Chem. Chem. Phys. **12**, 11062 (2010).
[43] M. A. Budroni, M. Rustici, and E. Tiezzi, Math. Model. Nat. Phenom. **6**, 226 (2011).
[44] E. L. Cussler, *Diffusion: Mass Transfer in Fluid Systems* (Cambridge University Press, Cambridge, New York, 2009).
[45] R. Krupiczka and A. Rotkegel, Chem. Eng. Sci. **52**, 1007 (1997).
[46] E. P. Zemskov, K. Kassner, and M. J. B. Hauser, Phys. Rev. E **77**, 036219 (2008).
[47] V. K. Vanag and I. R. Epstein, Phys. Chem. Chem. Phys. **11**, 897 (2009).
[48] E. P. Zemskov, V. K. Vanag, and I. R. Epstein, Phys. Rev. E **84**, 036216 (2011).
[49] F. Rossi, V. K. Vanag, and I. R. Epstein, Chem. Eur. J. **17**, 2138 (2011).
[50] E. P. Zemskov, K. Kassner, M. J. B. Hauser, and W. Horsthemke, Phys. Rev. E **87**, 032906 (2013).
[51] I. Berenstein and C. Beta, J. Chem. Phys. **136**, 034903 (2012).
[52] I. Berenstein and C. Beta, Chaos: Interdisc. J. Nonlin. Sci. **23**, 033119 (2013).
[53] B. N. Preston, T. C. Laurent, W. D. Comper, and G. J. Checkley, Nature **287**, 499 (1980).
[54] T. C. Laurent, B. N. Preston, W. D. Comper, G. J. Checkley, K. Edsman, and L. O. Sundelof, J. Phys. Chem. **87**, 648 (1983).
[55] W. D. Comper, G. J. Checkley, and B. N. Preston, J. Phys. Chem. **88**, 1068 (1984).
[56] W. D. Comper, G. J. Checkley, and B. N. Preston, J. Phys. Chem. **89**, 1551 (1985).
[57] W. D. Comper, R. P. W. Williams, G. J. Checkley, and B. N. Preston, J. Phys. Chem. **91**, 993 (1987).
[58] S. Sasaki, J. Phys. Chem. **100**, 20164 (1996).
[59] M. A. Budroni, L. Lemaigre, A. De Wit, and F. Rossi, Phys. Chem. Chem. Phys. **17**, 1593 (2015).
[60] M. A. Budroni, J. Carballido-Landeira, A. Intiso, A. De Wit, and F. Rossi, Chaos **25**, 064502 (2015).
[61] V. K. Vanag and D. V. Boulanov, J. Phys. Chem. **98**, 1449 (1994).
[62] V. K. Vanag and I. R. Epstein, Phys. Rev. Lett. **87**, 228301 (2001).
[63] V. K. Vanag and I. R. Epstein, Science **294**, 835 (2001).
[64] V. K. Vanag and I. R. Epstein, Proc. Natl. Acad. Sci. USA **100**, 14635 (2003).
[65] V. K. Vanag, Physics Uspekhi **47**, 923 (2004).
[66] F. Rossi, R. Varsalona, and M. L. T. Liveri, Chem. Phys. Lett. **463**, 378 (2008).
[67] T. P. d. Souza and J. Perez-Mercader, Chem. Commun. **50**, 8970 (2014).
[68] R. Tomasi, J.-M. Noel, A. Zenati, S. Ristori, F. Rossi, V. Cabuil, F. Kanoufi, and A. Abou-Hassan, Chem. Sci. **5**, 1854 (2014).
[69] L. Rongy, P. M. J. Trevelyan, and A. De Wit, Phys. Rev. Lett. **101**, 084503 (2008).
[70] D. W. Peaceman and H. H. Rachford, J. Soc. Ind. Appl. Math. **3**, 28 (1955).
[71] T. K. Sherwood and J. C. Wei, Ind. Eng. Chem. **49**, 1030 (1957).
[72] D. Avnir and M. Kagan, Nature **307**, 717 (1957).
[73] V. Loodts, C. Thomas, L. Rongy, and A. De Wit, Phys. Rev. Lett. **113**, 114501 (2014).